SIAM J. SCI. COMPUT.
Vol. 40, No. 5, pp. B1470–B1493

A PRECONDITIONED FINITE ELEMENT SOLUTION OF THE COUPLED PRESSURE-TEMPERATURE EQUATIONS USED TO MODEL TRACE GAS SENSORS*

ARTUR SAFIN†, SUSAN MINKOFF†, AND JOHN ZWECK†

Abstract. Quartz enhanced photoacoustic spectroscopy (QEPAS) is a technique for detecting trace gases which relies on a quartz tuning fork resonator to amplify and measure the weak acoustic pressure waves that are generated when a laser heat source periodically interacts with a gas sample. At low ambient pressures, the same tuning fork can instead detect thermal diffusion waves generated by this laser-gas interaction in a process called resonant optothermoacoustic detection (ROTADE). In this paper, we present a unified computational model for QEPAS and ROTADE sensors that is based on a coupled system of Helmholtz equations for pressure and temperature in a fluid domain surrounding the tuning fork. In the tuning fork itself, the standard heat equation is used to solve for temperature. We employ the perfectly matched layer (PML) approach to absorb outgoing waves and prevent reflections off of the boundary of the computational domain. The resulting linear system is highly ill conditioned, but Krylov subspace solvers can be used to solve the system effectively if one employs an appropriate parallel block preconditioner. This method reduces the problem to that of solving a scalar Helmholtz problem with PML, which we precondition by coupling an algebraic multigrid solver in the interior of the computational domain to a direct solver in the PML region. Numerical results indicate that the preconditioner for the scalar Helmholtz problem with PML is both scalable and mesh-independent. Simulations show that the coupled pressure-temperature waves can strongly differ from the solution to the acoustic wave equation at low ambient pressures. In particular, interactions between the pressure and temperature solutions of the coupled system contribute to the reduced sensitivity of ROTADE sensors which has been experimentally observed in certain parameter regimes.

Key words. block preconditioners, coupled pressure-temperature equations, Helmholtz equations, perfectly matched layer, photoacoustic spectroscopy, trace gas sensing

AMS subject classifications. 35J05, 35J57, 35K05, 35Q35, 65F08, 65N30

DOI. 10.1137/17M1145823

1. Introduction.

Laser absorption spectroscopy is a technique for detecting and measuring minute amounts of gases such as methane, carbon dioxide, and ethane. Trace gas sensing applications range from urban air quality monitoring to disease diagnosis via breath analysis to industrial process control [17, 46, 47]. One of the most robust and sensitive optical detection techniques for trace gas sensing is photoacoustic spectroscopy (PAS), which offers a cost-effective, compact, and versatile alternative to more traditional sensing methods [46]. A particular variant of PAS is quartz enhanced photoacoustic spectroscopy (QEPAS), which employs a quartz tuning fork (QTF) as an alternative to the traditional spectrophone [17, 32]. (See Figure 1(a) for a photograph of a QTFl.) Due to the small damping and the narrow bandwidth of the resonances of the QTF, QEPAS sensors are nearly immune to background noise and can detect gas concentrations in the parts per million to parts per billion

*Submitted to the journal's Computational Methods in Science and Engineering section September 1, 2017; accepted for publication (in revised form) August 16, 2018; published electronically October 30, 2018.

http://www.siam.org/journals/sisc/40-5/M114582.html

Funding: This work was supported by National Science Foundation grant DMS-1620293. The numerical simulations were performed on the Extreme Science and Engineering Discovery Environment (XSEDE), which is supported by National Science Foundation grant ACI-1548562.

†Department of Mathematical Sciences, The University of Texas at Dallas, Richardson, TX 75080 (artur.safin@utdallas.edu, sminkoff@utdallas.edu, zweck@utdallas.edu).

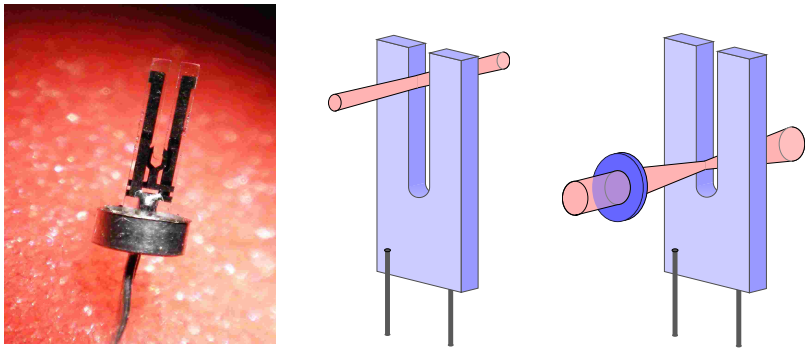

(a) (b) (c)

FIG. 1. (a) *Photograph of a quartz tuning fork with the size shown relative to a human finger (photo courtesy of A. Kosterev). Visualization of the experimental setup of* (b) *a QEPAS sensor and* (c) *a ROTADE sensor. The two schematic diagrams show the tuning fork (blue), laser source (pink), and electrode wires (black). For the ROTADE model, the laser beam is focused through a lens (dark blue). Color is available online only.*

range [19, 35, 55].

QEPAS sensors employ a modulated single-wavelength laser source to irradiate a gas sample, with the laser wavelength chosen to match an absorption line of a particular chemical species to be detected [40]. When the laser radiation is absorbed by the trace gas, the gas molecules release their excess vibrational energy as heat. Because the interaction between the laser and the trace gas is modulated at a prescribed frequency, the transport of vibrational energy is in the form of a thermal diffusion wave. In addition, vibrational-to-translational (V-T) energy conversion processes in the gas generate an acoustic pressure wave. Both the thermal and the acoustic waves induce a measurable response from the tuning fork, an effect that can be significantly enhanced if the modulation frequency of the laser source is chosen to excite a resonant vibration in the tuning fork. At the surface of the QTF the thermal wave dissipates into the interior of the tuning fork and induces a mechanical stress in the form of a deformation of its tines. Since quartz is a piezoelectric material [45], the vibration of the tines generates a current that can be measured on electrodes attached to the sides of the tuning fork [33, 45]. In addition, the acoustic pressure wave imparts a periodic forcing on the surface of the tuning fork that also induces a mechanical vibration of the QTF. This mechanical vibration then generates an additional electrical signal through the same piezoelectric effect. Thus, the QTF detects vibrations induced by both the pressure and the temperature waves, with the amplitude of the measured electric signal being proportional to the concentration of the trace gas [27, 34].

Although in theory the acoustic and thermal waves can both contribute to the measured signal, in practice the systems are usually designed so that only one of these phenomena dominates. When the acoustic wave is the dominant component of the signal, the system is referred to as a QEPAS sensor [32, 35], and when the thermal wave dominates, the system is referred to as a resonant optothermoacoustic detection (ROTADE) sensor [33]. However, experiments have also been performed in which both the thermal and the acoustic signals are significant [33, 49]. The primary factors dictating whether the QEPAS or ROTADE phenomena dominates are the position of the laser and the ambient pressure. QEPAS sensors typically operate in ambient pressure regimes ranging from 50 Torr ($\approx 1/15$ atm) to 1 atm [19, 46], with the laser

focused near the top of the QTF (see Figure 1(b)) [17]. Below 50 Torr, the rate of V-T relaxation becomes less significant and whether the acoustic or thermal wave dominates depends upon the position of the laser beam [33]. When the laser is focused near the bottom of the tines (see Figure 1(c)), the system acts as a ROTADE sensor.

Accurate mathematical models of QEPAS and ROTADE sensors are essential for optimizing their performance. Previous work by Petra et al. [49] employed a simplified computational model of a ROTADE sensor to numerically optimize the geometry of a QTF. Firebaugh, Terray, and Dong [23] developed a numerical model of a QEPAS sensor with a microresonator to predict the optimal dimensions of the microresonator tube. They later studied how sensor performance was affected by variations in QTF geometry [24]. A significant deficiency of these studies is the use of ad hoc damping models for the QTF derived from experimental data. For instance, Petra et al. [48, 49] relied on an experimentally measured quality factor to determine a damping coefficient in a model for the thermoelastic deformation of the QTF. To model damping accurately, viscous damping due to the motion of the QTF through the fluid (the main source of damping) must be included [4, 24, 44].

This paper is a major advance towards the development of a joint mathematical model that accurately incorporates viscous damping and thermal conduction effects for both QEPAS and ROTADE sensors. We present a computational model that describes the behavior of the acoustic and thermal waves due to a laser source in the presence of a QTF. Our model relies upon a coupled pressure-temperature system of Helmholtz equations derived by Morse and Ingard [42], which represents a generalization of the standard heat and acoustic wave equations and includes viscous damping and thermal conduction effects. A motivation for studying the coupled system is to analyze the nature of the interaction between the acoustic and thermal waves, which has been shown to be nontrivial in certain cases [33, 49].

This work builds on a recent publication by Kaderli et al. [30], in which we derived an analytic solution to the pressure-temperature equations in an infinitely long cylindrical tube of air surrounded by a solid annulus. The solution demonstrated that in certain parameter regimes there is a significant difference between the solution of the coupled pressure-temperature system and the solution of the classical heat equation. To facilitate the study of these physical effects, we develop a parallel preconditioned iterative scheme to solve the linear problem obtained from the finite element discretization of the pressure-temperature system. Brennan and Kirby [9] and Brennan et al. [10] studied related preconditioning schemes for the coupled pressure-temperature equations in the absence of a QTF on a rectangular domain with Dirichlet boundary conditions.

Our numerical results demonstrate the ability of our method to model both QEPAS and ROTADE sensors. In particular, we show that at low ambient pressures, the pressure solution to the coupled system behaves very differently from the solution of the classical wave equation. Our numerical results also provide an explanation for a discrepancy between the experimentally measured and numerically computed signals observed in Petra et al [48], which highlights the importance of realistic modeling of the interface between the air and the tuning fork domains. Our final simulation study suggests that an interaction between the pressure and temperature solutions of the coupled system contributes to the reduction in the sensitivity of ROTADE sensors that was experimentally observed by Kosterev and Doty [33] in certain parameter regimes.

We implement the PML method [8] to absorb the outgoing pressure and temperature waves at the boundaries of the computational domain. A considerable

amount of research has been dedicated toward developing efficient techniques for solving Helmholtz problems with PML. Erlangga [21] implemented a Krylov subspace solver preconditioned by a geometric multigrid F-cycle with a complex shift in the Laplacian operator. Approaches based on sweeping preconditioners have been studied in [20, 50]. In addition, a nested dissection method coupled with Dirichlet-to-Neumann maps has been investigated in [38], with nearly $\mathcal{O}(n)$-complexity for 2D problems. Finally, a survey of recent work based on the multifrontal method can be found in [54, 56].

In this paper, we introduce a novel approach for preconditioning indefinite scalar Helmholtz problems with PML, based on partitioning the domain into subregions with and without PML. In the non-PML region, we compute an approximate solution by solving the scalar Helmholtz problem with homogeneous Robin boundary conditions, which can then be used as boundary data for the PML region. A particular advantage of our approach over the methods in [20, 38, 50] is the ability to deal with unstructured, adaptively refined meshes that are graph partitioned for parallel computations. Our numerical scheme also benefits from the use of the algebraic multigrid method, which has been shown by Brennan and Kirby [9] to perform well for the coupled pressure-temperature equations in the non-PML region. Our numerical results demonstrate that the preconditioner for the Helmholtz problem with PML is scalable and is independent of the mesh size. We also prove that the number of nonunitary eigenvalues of the preconditioned system is bounded above by the number of unknowns on the interface between the computational domain and the PML region.

In section 2, we provide a brief description of the coupled pressure-temperature equations and describe our computational model of QEPAS and ROTADE sensors. In section 3, we discuss the preconditioner we developed for the Helmholtz problem with PML. In section 4, we derive a finite element discretization of the coupled pressure-temperature equations and describe the global preconditioning scheme. In section 5, we present numerical results that we obtained using our custom Helmholtz preconditioner and results for the global pressure-temperature problem. Finally, in section 6, we summarize our results and discuss future work.

2. Numerical model. To date, realistic mathematical modeling of trace gas sensors has focused on simplified models of either the thermal or the acoustic components of the process (Petra et al. [48, 49], Firebaugh, Terray, and Dong [23], and Firebaugh et al. [24]). In this paper, we study the unified *thermoacoustic* system of Morse and Ingard [42], which models a coupled pressure disturbance, P, and temperature disturbance, T, generated by a heat source, S. Our approach builds on previous work by Cao and Diebold [12], Brennan and Kirby [9], and Kaderli et al. [30]. This system, derived from the linearized Navier–Stokes equations by Morse and Ingard [42], is given by

$$\Delta P - \frac{\gamma}{c^2}\left(\frac{\partial^2}{\partial t^2} - \ell_v c \frac{\partial}{\partial t}\Delta\right)(P - \alpha T) = 0, \tag{2.1a}$$

$$\ell_h c \Delta T - \frac{\partial}{\partial t}\left(T - \frac{\gamma - 1}{\gamma\alpha}P\right) = -\frac{1}{\rho C_p}S. \tag{2.1b}$$

The parameters in system (2.1) are the isentropic expansion factor of the gas, γ, the speed of sound in the gas, c, the rate of change of pressure with respect to temperature at constant volume, α, the density, ρ, and the specific heat capacity, C_p. The constant $\ell_h = \kappa/(\rho c C_p)$ is the thermal characteristic length, where κ is thermal conductivity, and $\ell_v = \mu(4/3 + \eta/\mu)/(\rho c)$ is the characteristic length of viscosity, where η and μ

are the bulk and the dynamic viscosities of the fluid, respectively. The function, S, represents the heat power density deposited into the gas [41], which we model as a time-harmonic function of the form [48]

$$S(\mathbf{x},t) = \frac{\alpha_{\text{eff}} W_L}{\pi w^2(y)} \exp\left[-\frac{2[(x-x_s)^2+(z-z_s)^2]}{w^2(y)}\right]\cos(\omega t), \tag{2.2}$$

where the constant α_{eff} is the effective absorption coefficient of the gas, W_L is the total laser power, and ω is the angular frequency of the laser. The laser beam is aligned with the y-axis, and is focused at the point (x_s, y_s, z_s), where y_s is halfway between the front and back faces of the tuning fork. The function $w(y)$ is the width of the laser beam, which for ROTADE sensors is given by [49]

$$w(y) = \sigma\sqrt{1+\left(\frac{y-y_s}{y_R}\right)^2}, \tag{2.3}$$

where σ is the beam width at the focal point, and $y_R = \pi\sigma^2/\lambda$ is the Rayleigh length, with λ being the wavelength of radiation [53]. For QEPAS sensors [48], the width of the beam is modeled by the constant $w(y) = \sigma$.

2.1. Helmholtz version of thermoacoustic equations. Since the laser operates at a single frequency, the solution to the thermoacoustic equations (2.1) is time-harmonic, with the pressure, temperature, and laser source being of the form

$$P(\mathbf{x},t) = \Re e\left[P(\mathbf{x})e^{-i\omega t}\right], \quad T(\mathbf{x},t) = \Re e\left[T(\mathbf{x})e^{-i\omega t}\right], \quad S(\mathbf{x},t) = \Re e\left[S(\mathbf{x})e^{-i\omega t}\right]. \tag{2.4}$$

Under this assumption, we obtain a coupled system of Helmholtz equations,

$$\Delta P + \frac{\gamma}{c^2}(\omega^2 - i\ell_v c\omega\Delta)(P - \alpha T) = 0, \tag{2.5a}$$

$$\ell_h c\Delta T + i\omega\left(T - \frac{\gamma-1}{\gamma\alpha}P\right) = -\frac{1}{\rho C_p}S, \tag{2.5b}$$

where the functions P, T, and S now depend only on the spatial variable $\mathbf{x}$.

We now reformulate the thermoacoustic equations (2.5) by using (2.5b) to eliminate ΔT from (2.5a). We also rewrite (2.5b) in a form such that the coefficient of ΔT is thermal conductivity κ to obtain

$$\xi\Delta P + a_1 P + a_2 T = ia_3 S, \tag{2.6a}$$

$$\kappa\Delta T + ib_2 T - ib_1 P = -S. \tag{2.6b}$$

Except for ξ, the constants in system (2.6) are all real and positive and are given by

$$\begin{aligned} a_1 &= k^2\left(\gamma - \frac{\ell_v}{\ell_h}(\gamma-1)\right), & a_2 &= k^2\gamma\alpha\left(\frac{\ell_v}{\ell_h}-1\right), & a_3 &= \frac{\gamma\alpha k^2}{\omega\rho C_p}\frac{\ell_v}{\ell_h}, \\ b_1 &= \rho C_p\frac{\omega(\gamma-1)}{\gamma\alpha}, & b_2 &= \omega\rho C_p, & & \\ k &= \frac{\omega}{c}, & \xi &= 1 - i\gamma k\ell_v. & & \end{aligned} \tag{2.7}$$

For trace gas sensors, $k \approx 500$ [32], and so in (2.6a), a_1 and a_2 are both large, with a_2 being two orders of magnitude greater than a_1 for QEPAS sensors. The parameter ξ is a small perturbation of 1, and a_3 is small. In (2.6b), b_1 and b_2 are large constants in comparison to thermal diffusivity constant κ.

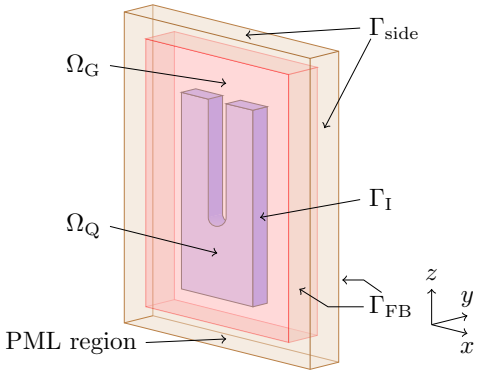

FIG. 2. *Domain for the numerical simulation of the thermoacoustic equations in the presence of a QTF. The tuning fork is shaded purple, and the surrounding gas is colored pink. The absorbing boundary layer is shaded tan and is only implemented in the x- and z-directions. Color is available online only.*

2.2. Boundary and interface conditions. We solve the thermoacoustic system (2.6) in a fluid domain, Ω_{G}, that surrounds a QTF, Ω_{Q}, chosen so that $\Omega = \Omega_{\text{G}} \cup \Omega_{\text{Q}}$ is a box. To prevent artificial reflections off the boundary of the box, we include an absorbing boundary layer as shown in Figure 2. We denote the front and back faces (parallel to the xz-plane) of Ω by Γ_{FB}, the side faces (perpendicular to the xz-plane) by Γ_{side}, and the interface between the tuning fork and fluid by Γ_{I}. The boundary of Ω_{G} is therefore given by $\Gamma = \Gamma_{\text{I}} \cup \Gamma_{\text{side}} \cup \Gamma_{\text{FB}}$.

On the boundary of the tuning fork, we impose zero Neumann boundary conditions for pressure,

$$\nabla P \cdot \mathbf{n} = 0, \tag{2.8}$$

where $\mathbf{n}$ is the normal vector. Here, for the purpose of modeling the acoustic and thermal waves, we have assumed that the surface of the tuning fork is rigid. This assumption is reasonable since the amplitude of the vibration of the tuning fork is several orders of magnitude smaller than the characteristic lengths of the system.

We model the temperature, T_Q, in the interior of the tuning fork using the Helmholtz form of the classical heat equation,

$$\nabla \cdot (\boldsymbol{\kappa_Q} \nabla T_Q) + ic_1 T_Q = 0 \quad \text{in } \Omega_{\text{Q}}, \tag{2.9}$$

where $\boldsymbol{\kappa_Q} = \text{diag}(\kappa_1, \kappa_2, \kappa_3)$ is the diagonal thermal conductivity tensor of quartz, and $c_1 = \omega \rho_Q C_{p,Q}$, with ρ_Q and $C_{p,Q}$ being the density and the specific heat capacity of quartz, respectively. We couple (2.5b) and (2.9) using the interface conditions on Γ_{I},

$$\begin{cases} T(\mathbf{x}) = T_Q(\mathbf{x}) & \text{(continuity of heat)}, \\ \kappa(\nabla T \cdot \mathbf{n}) = (\boldsymbol{\kappa_Q} \nabla T_Q) \cdot \mathbf{n} & \text{(continuity of flux)}. \end{cases} \tag{2.10}$$

Since the laser beam passes through the front and back faces of the box, we require different boundary conditions on Γ_{FB} than on Γ_{side}. Provided that the front and back faces are sufficiently far from the QTF, near Γ_{FB} the thermoacoustic waves mostly propagate outward from the axis of the beam. Therefore, we assume that the

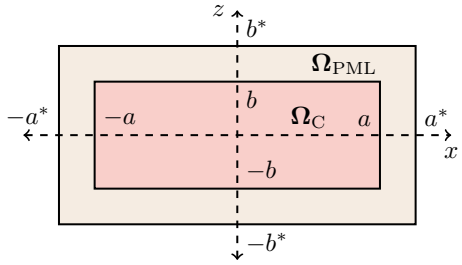

FIG. 3. *A 2D model of a computational domain Ω_C surrounded by an absorbing layer Ω_{PML}. Since the solution decays exponentially, zero Dirichlet boundary conditions on the outer boundary Γ_{side} of the PML region are sufficient.*

boundary condition on Γ_{FB} is given by the solution, $(P_{\mathrm{FB}}, T_{\mathrm{FB}})$, to the 2D thermoacoustic equations on Γ_{FB}. To be compatible with the 3D problem, we also include an absorbing layer on the edges of the front and back faces.

To model the absorbing layer of the 3D box, Ω, we apply the PML method of Berenger [8] to the lateral faces, Γ_{side}. Berenger's idea was to surround the computational domain by an additional layer of absorbing material designed to exponentially attenuate all outgoing waves. In Figure 3, we show a typical 2D domain for PML. Berenger's original formulation of the PML method was reformulated by Chew and Weedon [14] in terms of complex coordinate stretching. Using this approach, Lassas and Somersalo [36] proved that the solution in a finite domain surrounded by PML converges exponentially to the true solution with Sommerfeld radiation conditions as the width of the absorbing layer tends to infinity. The complex stretching in the x-direction can be achieved by replacing the partial differential operator $\frac{\partial}{\partial x}$ by $\frac{1}{\beta_x(x)}\frac{\partial}{\partial x}$, where [14]

$$\beta_x = \beta_x(x) = \begin{cases} 1 & \text{for } |x| \le a, \\ 1 + \dfrac{i}{\omega}\sigma_x(x) & \text{for } a < |x| \le a^*. \end{cases} \tag{2.11}$$

We chose the function $\sigma_x(x)$, which determines the rate at which the solution decays in the absorbing layer, to be

$$\sigma_x(x) = A\frac{(x-a)^2}{(a^*-a)^2}, \tag{2.12}$$

where the choice $A = 50\,\omega$ gave a satisfactory performance for the mesh we used. We implement PML in the z-direction similarly, but in the y-direction we use the boundary conditions on Γ_{FB} given above.

Since heat dissipates rapidly, the standard approach for modeling heat phenomena is to impose zero boundary conditions at a sufficient distance from thermal sources. However, due to the coupling with the acoustic wave, such boundary conditions may no longer be appropriate. To better understand the far-field behavior of the coupled system, in supplementary section SM1 we derive a cylindrically symmetric solution to the thermoacoustic equations in all of $\mathbb{R}^3$ for a laser beam of constant width. The formula we obtain shows that *in the far field, the temperature decays at a rate proportional to the pressure*, which indicates that we need to implement PML for both pressure and temperature. Therefore, with the inclusion of PML, the thermoacoustic

system (2.6) becomes

$$\xi\,(\nabla\cdot\mathbf{B}(\mathbf{x})\nabla P)+a_1\beta_x\beta_z P+a_2\beta_x\beta_z T=ia_3\beta_x\beta_z S, \tag{2.13a}$$

$$\kappa\,(\nabla\cdot\mathbf{B}(\mathbf{x})\nabla T)+ib_2\beta_x\beta_z T-ib_1\beta_x\beta_z P=-\beta_x\beta_z S, \tag{2.13b}$$

where $\mathbf{B}(\mathbf{x})=\mathrm{diag}[\beta_z\beta_x^{-1},\,\beta_x\beta_z,\,\beta_x\beta_z^{-1}]$.

3. A preconditioner for a scalar Helmholtz problem with PML. In section 4, we will describe the block preconditioner that we use to solve the entire system of equations for pressure and temperature in the gas (2.13) and temperature in the tuning fork (2.9). This method reduces the problem to that of solving a Helmholtz problem with PML for a single unknown (either pressure or temperature), of the form

$$\begin{cases}\nabla\cdot(\mathbf{B}(\mathbf{x})\nabla u)+\beta_x\beta_y k^2u=f, & \mathbf{x}\in\Omega,\\ u=0, & \mathbf{x}\in\partial\Omega,\end{cases} \tag{3.1}$$

where Ω is a box in $\mathbb{R}^2$ or $\mathbb{R}^3$. As in Figure 3, we assume that $\Omega=\Omega_{\mathrm{C}}\cup\Omega_{\mathrm{PML}}$ is the disjoint union of the computational domain, Ω_{C}, and the PML region, Ω_{PML}. In subsections 3.1 and 3.2, we derive a finite element version of the preconditioner for the subdomains, and in subsection 3.3, we show how this preconditioner can be applied to the global problem.

3.1. Continuous approximation. We begin by formulating the continuous version of the preconditioner. We partition the global problem (3.1) into subproblems over the computational domain Ω_{C} and the PML region Ω_{PML},

$$\begin{cases}\Delta v+k^2v=f, & \mathbf{x}\in\Omega_{\mathrm{C}},\\ ikv+\nabla v\cdot\mathbf{n}=ikw+\nabla w\cdot\mathbf{n}, & \mathbf{x}\in\mathcal{I},\end{cases} \tag{3.2}$$

$$\begin{cases}\nabla\cdot(\mathbf{B}(\mathbf{x})\nabla w)+\beta_x\beta_y k^2w=f, & \mathbf{x}\in\Omega_{\mathrm{PML}},\\ ikw+\nabla w\cdot\mathbf{n}=ikv+\nabla v\cdot\mathbf{n}, & \mathbf{x}\in\mathcal{I},\\ w=0, & \mathbf{x}\in\partial\Omega,\end{cases} \tag{3.3}$$

where $\mathcal{I}=\overline{\Omega}_{\mathrm{C}}\cap\overline{\Omega}_{\mathrm{PML}}$ is the interface between the computational and PML regions. It can be shown [51] that the solution of the original problem (3.1) is equivalent to the solution of the coupled system (3.2) and (3.3), with

$$u=\begin{cases}v, & \mathbf{x}\in\Omega_{\mathrm{C}},\\ w, & \mathbf{x}\in\Omega_{\mathrm{PML}}.\end{cases} \tag{3.4}$$

Instead of solving (3.2) and (3.3) simultaneously, we obtain an approximate solution by first solving a simplified problem for v in Ω_{C} and then feeding the solution into (3.3) and solving for w. Specifically, we first solve the problem in the computational domain with zero right-hand side for the transmission conditions, given by

$$\begin{cases}\Delta v+k^2v=f, & \mathbf{x}\in\Omega_{\mathrm{C}},\\ ikv+\nabla v\cdot\mathbf{n}=\mathbf{0}, & \mathbf{x}\in\mathcal{I}.\end{cases} \tag{3.5}$$

This subproblem is also well-posed under the assumption that k^2 is not a generalized eigenvalue of the system [1]. This approximation is a common approach for imposing reasonable but not exact boundary conditions for Helmholtz problems [22, 37]. The solution to (3.5) is then fed into the exterior problem (3.3) as a boundary condition on the interface:

$$\begin{cases}\nabla\cdot(\mathbf{B}(\mathbf{x})\nabla w)+\beta_x\beta_y k^2w=f, & \mathbf{x}\in\Omega_{\mathrm{PML}},\\ w=v, & \mathbf{x}\in\mathcal{I}.\end{cases} \tag{3.6}$$

3.2. Matrix formulation. We now focus on the linear algebra formulation of the problems given in (3.5) and (3.6). The variational problem for (3.5) is to find a solution $v \in \mathrm{H}^1(\Omega_{\mathrm{C}})$ such that

$$-\int_{\Omega_{\mathrm{C}}} \nabla v \cdot \nabla q \, d\mathbf{x} + k^2 \int_{\Omega_{\mathrm{C}}} vq \, dx + ik \int_{\mathcal{I}} vq \, ds = \int_{\Omega_{\mathrm{C}}} fq \, d\mathbf{x} \tag{3.7}$$

for all $q \in \mathrm{H}^1(\Omega_{\mathrm{C}})$, which, using the finite element method, gives rise to a linear system of the form

$$\widetilde{\mathbf{H}}_{\mathrm{C}}\mathbf{v} = \widetilde{\mathbf{M}}_{\mathrm{C}}\mathbf{f}_{\mathrm{C}}, \tag{3.8}$$

where $\widetilde{\mathbf{M}}_{\mathrm{C}}$ is the mass matrix assembled over the computational domain, and $\widetilde{\mathbf{H}}_{\mathrm{C}}$ is obtained from the discretization of the left-hand side of the variational problem (3.7).

In the PML region, we only need to solve (3.6) for the unknowns on the interior of Ω_{PML} since the values of w on the interface $\mathcal{I}$ are supplied by the Dirichlet boundary condition. However, instead of solving the exterior problem (3.6) directly, we can use the global formulation (3.1) to obtain an equivalent solution in the PML region where we impose the additional condition that $u = v$ in $\overline{\Omega}_{\mathrm{C}}$. Specifically, suppose we have discretized (3.1) as

$$\mathbf{H}\mathbf{u} = \mathbf{M}\mathbf{f} = \mathbf{b}, \tag{3.9}$$

where $\mathbf{M}$ is the mass matrix over the entire domain Ω, and $\mathbf{H}$ is the discretization of the Helmholtz operator in (3.1). If we write $\mathbf{u}$ as $\mathbf{u}^{\mathrm{T}} = \left[\mathbf{v}^{\mathrm{T}} \ \mathbf{w}_{\mathrm{E}}{}^{\mathrm{T}}\right]$, where $\mathbf{v}$ are the entries corresponding to basis functions whose support intersects Ω_{C}, and similarly decompose $\mathbf{f}^{\mathrm{T}} = \left[\mathbf{f}_{\mathrm{C}}^{\mathrm{T}} \ \mathbf{f}_{\mathrm{E}}^{\mathrm{T}}\right]$, then the linear system (3.9) can be partitioned as

$$\begin{bmatrix} \mathbf{H}_{\mathrm{C}} & \mathbf{H}_{\mathrm{CE}} \\ \mathbf{H}_{\mathrm{EC}} & \mathbf{H}_{\mathrm{E}} \end{bmatrix} \begin{bmatrix} \mathbf{v} \\ \mathbf{w}_{\mathrm{E}} \end{bmatrix} = \begin{bmatrix} \mathbf{M}_{\mathrm{C}} & \mathbf{M}_{\mathrm{CE}} \\ \mathbf{M}_{\mathrm{EC}} & \mathbf{M}_{\mathrm{E}} \end{bmatrix} \begin{bmatrix} \mathbf{f}_{\mathrm{C}} \\ \mathbf{f}_{\mathrm{E}} \end{bmatrix}. \tag{3.10}$$

We emphasize here that the solution to system (3.10) is a finite element solution of the original Helmholtz problem with PML given by (3.1). Since we have an approximation of $\mathbf{v}$ available as the solution of the linear system (3.8), we can use it to obtain $\mathbf{w}_{\mathrm{E}}$ from the second row in (3.10). Specifically, we just need to solve for $\mathbf{w}_{\mathrm{E}}$ in

$$\mathbf{H}_{\mathrm{E}}\mathbf{w}_{\mathrm{E}} = (\mathbf{M}_{\mathrm{EC}}\mathbf{f}_{\mathrm{C}} + \mathbf{M}_{\mathrm{E}}\mathbf{f}_{\mathrm{E}}) - \mathbf{H}_{\mathrm{EC}}\mathbf{v}. \tag{3.11}$$

Thus, the approximate solution to linear system (3.9) on Ω is given by (3.8) and (3.11), namely

$$\begin{bmatrix} \mathbf{v} \\ \mathbf{w}_{\mathrm{E}} \end{bmatrix} = \begin{bmatrix} \widetilde{\mathbf{H}}_{\mathrm{C}}^{-1}\widetilde{\mathbf{M}}_{\mathrm{C}}\mathbf{f}_{\mathrm{C}} \\ \mathbf{H}_{\mathrm{E}}^{-1}\left[(\mathbf{M}_{\mathrm{EC}}\mathbf{f}_{\mathrm{C}} + \mathbf{M}_{\mathrm{E}}\mathbf{f}_{\mathrm{E}}) - \mathbf{H}_{\mathrm{EC}}\mathbf{v}\right] \end{bmatrix}. \tag{3.12}$$

3.3. Preconditioner. In this subsection, we demonstrate how the approximate solution (3.12) can be used to formulate a preconditioner, $\mathbf{P}$, for the entire system (3.9). An important consideration here is that the implementation of the GMRES algorithm [52] requires us to apply the preconditioner to vectors in the Krylov subspace[1]

$$\mathcal{K}_i(\mathbf{H}\mathbf{P}^{-1}, \mathbf{b}) = \mathrm{span}\left\{\mathbf{b}, \ (\mathbf{H}\mathbf{P}^{-1})\mathbf{b}, \ (\mathbf{H}\mathbf{P}^{-1})^2\mathbf{b}, \ldots, \ (\mathbf{H}\mathbf{P}^{-1})^{i-1}\mathbf{b}\right\}. \tag{3.13}$$

[1]The sequence of iterates shown is for the *right*-preconditioned GMRES method. Due to spectral equivalence, however, left preconditioning typically exhibits the same rate of convergence [52].

Algorithm 1 Preconditioner for a scalar Helmholtz problem with PML: $\mathbf{u} = \mathbf{P}^{-1}\mathbf{b}$

1: Initialize auxiliary vector $\mathbf{z}$ of the same size as $\mathbf{u}$
2: Solve $\mathbf{M}\mathbf{z} = \mathbf{b}$ using the conjugate gradient (CG) method
3: Extract $\mathbf{z}_{\mathrm{C}}$ from $\mathbf{z}$ and compute $\mathbf{z}_{\mathrm{C}} = \widetilde{\mathbf{M}}_C\mathbf{z}_{\mathrm{C}}$
4: Solve $\widetilde{\mathbf{H}}_{\mathrm{C}}\mathbf{v} = \mathbf{z}_{\mathrm{C}}$ using GMRES
with the AMG preconditioner ▷ Gives solution on $\overline{\Omega}_{\mathrm{C}}$
5: Compute $\mathbf{z}_{\mathrm{E}} = \mathbf{b}_{\mathrm{E}} - \mathbf{H}_{\mathrm{EC}}\mathbf{v}$
6: Solve $\mathbf{H}_{\mathrm{E}}\mathbf{w}_{\mathrm{E}} = \mathbf{z}_{\mathrm{E}}$ using sparse LU ▷ Gives solution on $\mathrm{int}(\Omega_{\mathrm{PML}})$
7: Return $\mathbf{u} = \begin{bmatrix} \mathbf{v} \\ \mathbf{w}_{\mathrm{E}} \end{bmatrix}$

Assuming we start with zero as our initial guess for the solution, the first vector in the Krylov subspace can be written as a product of the mass matrix with the discretized function f:

$$\mathbf{b} = \begin{bmatrix} \mathbf{b}_{\mathrm{C}} \\ \mathbf{b}_{\mathrm{E}} \end{bmatrix} = \mathbf{M}\mathbf{f} = \begin{bmatrix} \mathbf{M}_{\mathrm{C}} & \mathbf{M}_{\mathrm{CE}} \\ \mathbf{M}_{\mathrm{EC}} & \mathbf{M}_{\mathrm{E}} \end{bmatrix} \begin{bmatrix} \mathbf{f}_{\mathrm{C}} \\ \mathbf{f}_{\mathrm{E}} \end{bmatrix}. \tag{3.14}$$

We assume that all other vectors in the Krylov subspaces (3.13) have a similar form (i.e., mass matrix times a right-hand side vector). In this case, it is sufficient to show how to apply the preconditioner to $\mathbf{b}$. First, we observe that the solution in the computational domain is given by linear system (3.8), which, using (3.14), can be expressed in block form as

$$\begin{bmatrix} \mathbf{v} \\ \mathbf{0} \end{bmatrix} = \begin{bmatrix} \widetilde{\mathbf{H}}_{\mathrm{C}}^{-1}\widetilde{\mathbf{M}}_{\mathrm{C}}\mathbf{f}_{\mathrm{C}} \\ \mathbf{0} \end{bmatrix} = \begin{bmatrix} \widetilde{\mathbf{H}}_{\mathrm{C}}^{-1} & \mathbf{0} \\ \mathbf{0} & \mathbf{0} \end{bmatrix} \begin{bmatrix} \widetilde{\mathbf{M}}_{\mathrm{C}} & \mathbf{0} \\ \mathbf{0} & \mathbf{0} \end{bmatrix} \mathbf{M}^{-1}\mathbf{b}. \tag{3.15}$$

Having obtained $\mathbf{v}$, we compute $\mathbf{w}_{\mathrm{E}}$ using (3.11), noting that $\mathbf{M}_{\mathrm{EC}}\mathbf{f}_{\mathrm{C}} + \mathbf{M}_{\mathrm{E}}\mathbf{f}_{\mathrm{E}} = \mathbf{b}_{\mathrm{E}}$. The resulting solution can be equivalently expressed as

$$\begin{bmatrix} \mathbf{v} \\ \mathbf{w}_{\mathrm{E}} \end{bmatrix} = \mathbf{P}^{-1}\mathbf{b} = \begin{bmatrix} \widetilde{\mathbf{H}}_{\mathrm{C}}^{-1} & \mathbf{0} \\ -\mathbf{H}_{\mathrm{E}}^{-1}\mathbf{H}_{\mathrm{EC}}\widetilde{\mathbf{H}}_{\mathrm{C}}^{-1} & \mathbf{H}_{\mathrm{E}}^{-1} \end{bmatrix} \begin{bmatrix} \widetilde{\mathbf{M}}_{\mathrm{C}} & \mathbf{0} \\ \mathbf{M}_{\mathrm{EC}} & \mathbf{M}_{\mathrm{E}} \end{bmatrix} \mathbf{M}^{-1}\mathbf{b}. \tag{3.16}$$

The derivation above gives rise to Algorithm 1, which follows naturally from (3.15) and the second row in (3.12). In the algorithm, we also list the solvers that we have used for the particular linear subproblems. In step 2, we use the conjugate gradient method since the mass matrix is symmetric positive-definite. In step 4, we use the GMRES method preconditioned with algebraic multigrid (AMG), which has been shown to work well for this class of problems [9]. Finally, we use a direct solver for the highly indefinite Helmholtz problem in Ω_{PML}, where we reduce the number of unknowns using adaptive mesh refinement and choose a large coefficient for the attenuation function (2.12).

We now provide an estimate of the number of nonunitary eigenvalues of $\mathbf{P}^{-1}\mathbf{H}$. This result shows that GMRES converges to the solution of the preconditioned system in a number of iterations that is much smaller than the global size of the problem.

THEOREM 3.1. *Let $\mathcal{V}$ be the finite element space used to obtain the discretized linear system* (3.9)*. Then the number of nonunitary eigenvalues of $\mathbf{P}^{-1}\mathbf{H}$ is at most equal to the dimension of $\mathcal{V}_{\mathcal{I}} := \mathrm{span}\{\phi_i \in \mathcal{V} : \phi_i \cap \mathcal{I} \neq \varnothing\}$.*

Proof. Rather than focusing on $\mathbf{P}^{-1}\mathbf{H}$, we instead study $\mathbf{H}\mathbf{P}^{-1}$, which has an equivalent spectrum [52]. Using (3.10) and (3.16), we can obtain an explicit formulation of this operator as

$$\mathbf{H}\mathbf{P}^{-1} = \begin{bmatrix} \mathbf{Q} & \mathbf{Q}\mathbf{M}_{\mathrm{CE}}\mathbf{M}_{\mathrm{E}}^{-1} + \mathbf{H}_{\mathrm{CE}}\mathbf{H}_{\mathrm{E}}^{-1} \\ 0 & \mathbf{I} \end{bmatrix}, \tag{3.17}$$

where $\mathbf{Q} = \mathbf{S}_{\mathrm{H}}\widetilde{\mathbf{H}}_{\mathrm{C}}^{-1}\widetilde{\mathbf{M}}_{\mathrm{C}}\mathbf{S}_{\mathrm{M}}^{-1}$ is defined in terms of the invertible Schur complements $\mathbf{S}_{\mathrm{H}} = \mathbf{H}_{\mathrm{C}} - \mathbf{H}_{\mathrm{CE}}\mathbf{H}_{\mathrm{E}}^{-1}\mathbf{H}_{\mathrm{EC}}$ and $\mathbf{S}_{\mathrm{M}} = \mathbf{M}_{\mathrm{C}} - \mathbf{M}_{\mathrm{CE}}\mathbf{M}_{\mathrm{E}}^{-1}\mathbf{M}_{\mathrm{EC}}$.

We now show that $\mathbf{S}_{\mathrm{H}}$ and $\widetilde{\mathbf{H}}_{\mathrm{C}}$ differ only in the rows and columns that correspond to $\mathcal{V}_{\mathcal{I}}$. Let $\mathcal{V} = \mathcal{V}_{\mathrm{C}} \oplus \mathcal{V}_{\mathrm{E}}$, where $\mathcal{V}_{\mathrm{C}} = \mathrm{span}\{\phi_i \in \mathcal{V} : \mathrm{supp}(\phi_i) \cap \Omega_{\mathrm{C}} \neq \varnothing\}$ and $\mathcal{V}_{\mathrm{E}} = \mathrm{span}\{\phi_i \in \mathcal{V} : \mathrm{supp}(\phi_i) \cap \Omega_{\mathrm{C}} = \varnothing\}$. Then for any $\phi_i \in \mathcal{V}_{\mathrm{E}}$ and $\phi_j \in \mathcal{V}_{\mathrm{C}} \backslash \mathcal{V}_{\mathcal{I}}$ we have

$$(\mathbf{H}_{\mathrm{EC}})_{ij} = a(\phi_i, \phi_j)_{\Omega} = a(\phi_i, \phi_j)_{\Omega_{\mathrm{C}}} + a(\phi_i, \phi_j)_{\Omega_{\mathrm{PML}}} = 0, \tag{3.18}$$

where $a(\cdot,\cdot)_{\Lambda}$ is the variational form of (3.1) on some domain Λ. Since $(\mathbf{H}_{\mathrm{EC}})_{ij}$ is only nonzero if $\phi_j \in \mathcal{V}_{\mathcal{I}}$, we further partition $\mathbf{H}_{\mathrm{EC}} = \begin{bmatrix} \mathbf{0} & \mathbf{H}_{\mathrm{E}\mathcal{I}} \end{bmatrix}$, where the columns of $\mathbf{H}_{\mathrm{E}\mathcal{I}}$ correspond to basis functions in $\mathcal{V}_{\mathcal{I}}$. Using this formulation, we obtain

$$\mathbf{H}_{\mathrm{CE}}\mathbf{H}_{\mathrm{E}}^{-1}\mathbf{H}_{\mathrm{EC}} = \begin{bmatrix} \mathbf{0} \\ \mathbf{H}_{\mathcal{I}\mathrm{E}} \end{bmatrix} \mathbf{H}_{\mathrm{E}}^{-1} \begin{bmatrix} \mathbf{0} & \mathbf{H}_{\mathrm{E}\mathcal{I}} \end{bmatrix} = \begin{bmatrix} \mathbf{0} & \mathbf{0} \\ \mathbf{0} & \star \end{bmatrix}, \tag{3.19}$$

and hence

$$\mathbf{S}_{\mathrm{H}} - \mathbf{H}_{\mathrm{C}} = -\mathbf{H}_{\mathrm{CE}}\mathbf{H}_{\mathrm{E}}^{-1}\mathbf{H}_{\mathrm{EC}} = \begin{bmatrix} \mathbf{0} & \mathbf{0} \\ \mathbf{0} & \star \end{bmatrix}. \tag{3.20}$$

Next, we observe that $\widetilde{\mathbf{H}}_{\mathrm{C}}$ also differs from $\mathbf{H}_{\mathrm{C}}$ in the same $(2,2)$-block since

$$\begin{aligned} (\mathbf{H}_{\mathrm{C}} - \widetilde{\mathbf{H}}_{\mathrm{C}})_{ij} &= \left[a(\phi_i, \phi_j)_{\Omega}\right] - \left[a(\phi_i, \phi_j)_{\Omega_{\mathrm{C}}} + ik\int_{\mathcal{I}} \phi_i\phi_j \, ds\right] \\ &= a(\phi_i, \phi_j)_{\Omega_{\mathrm{PML}}} - ik\int_{\mathcal{I}} \phi_i\phi_j \, ds = 0 \end{aligned} \tag{3.21}$$

if either $\phi_i \notin \mathcal{V}_{\mathcal{I}}$ or $\phi_j \notin \mathcal{V}_{\mathcal{I}}$. Combining the results in (3.20) and (3.21), we find that $\mathbf{S}_{\mathrm{H}}$ and $\widetilde{\mathbf{H}}_{\mathrm{C}}$ only differ in the $(2,2)$-block, as do $\widetilde{\mathbf{M}}_{\mathrm{C}}$ and $\mathbf{S}_{\mathrm{M}}$ by the same argument. Therefore,

$$\mathbf{Q} = \left(\mathbf{S}_{\mathrm{H}}\widetilde{\mathbf{H}}_{\mathrm{C}}^{-1}\right)\left(\widetilde{\mathbf{M}}_{\mathrm{C}}\mathbf{S}_{\mathrm{M}}^{-1}\right) = \begin{bmatrix} \mathbf{I} & \star \\ \mathbf{0} & \star \end{bmatrix}\begin{bmatrix} \mathbf{I} & \star \\ \mathbf{0} & \star \end{bmatrix} = \begin{bmatrix} \mathbf{I} & \star \\ \mathbf{0} & \mathbf{Q}_{\mathcal{I}} \end{bmatrix}. \tag{3.22}$$

Taking advantage of the triangular structures in (3.17) and (3.22), we conclude that

$$p(\lambda) = \det(\mathbf{H}\mathbf{P}^{-1} - \lambda\mathbf{I}) = (\lambda - 1)^{\dim(\mathcal{V}) - \dim(\mathcal{V}_{\mathcal{I}})} \det(\mathbf{Q}_{\mathcal{I}} - \lambda\mathbf{I}). \tag{3.23}$$

Hence eigenvalue $\lambda = 1$ has an algebraic multiplicity of at least $\dim(\mathcal{V}) - \dim(\mathcal{V}_{\mathcal{I}})$, and therefore the number of nonunitary eigenvalues is at most $\dim(\mathcal{V}_{\mathcal{I}})$. ∎

The theorem above shows that the preconditioned operator is block upper triangular with $\mathrm{diag}(\mathbf{H}\mathbf{P}^{-1}) = \{\mathbf{I}, \mathbf{Q}, \mathbf{I}\}$, where $\dim(\mathbf{Q}) = \dim(\mathcal{V}_{\mathcal{I}})$. Hence we can show that the degree of the minimal polynomial [43, 52] of this preconditioned operator is at most $\dim(\mathcal{V}_{\mathcal{I}}) + 2$, and therefore the preconditioned operator converges to the solution in at most a number of iterations that is roughly equal to the size of the interface.

COROLLARY 3.2. *The GMRES algorithm applied to the preconditioned linear system* $\mathbf{HP}^{-1}\mathbf{x} = \mathbf{b}$ *converges to the solution in at most* $\dim(\mathcal{V}_\mathcal{I}) + 2$ *iterations.*

Similar theoretical results for the overlapping multiplicative Schwarz preconditioner are established in Kahou, Kamgnia, and Philippe [31]. We finally note that the bound in Corollary 3.2 is not tight since the numerical results in subsection 5.1 demonstrate that the preconditioned operator converges to the solution in just a few iterations.

4. Finite element discretization. In this section, we derive a global linear system that represents the finite element discretization of the thermoacoustic equations (2.13) and the heat equation (2.9), with couplings provided by the continuity conditions given in (2.10). The relevant subdomains and boundaries are defined in subsection 2.2. For the thermoacoustic equations, we seek to obtain solutions (P, T_G) in a finite element space

$$\mathcal{W}_\mathrm{G} = \mathrm{H}^1_0(\Omega_\mathrm{G}) \times \mathrm{H}^1_0(\Omega_\mathrm{G}), \tag{4.1}$$

where H^1_0 represents the Sobolev space of complex-valued functions

$$\mathrm{H}^1_0(\Omega_\mathrm{G}) = \left\{ u(\mathbf{x}) \in \mathrm{L}^2(\Omega_\mathrm{G}) \;\middle|\; \nabla u \in \mathrm{L}^2(\Omega_\mathrm{G}),\ u(\mathbf{x}) = 0 \text{ for } \mathbf{x} \in \Gamma_\mathrm{side} \cup \Gamma_\mathrm{FB} \right\}. \tag{4.2}$$

Here we do not require the functions in $\mathcal{W}_\mathrm{G}$ to be zero on Γ_I. For the tuning fork, the corresponding space is

$$\mathcal{W}_\mathrm{Q} = \mathrm{H}^1(\Omega_\mathrm{Q}) = \left\{ u(\mathbf{x}) \in \mathrm{L}^2(\Omega_\mathrm{Q}) \;\middle|\; \nabla u \in \mathrm{L}^2(\Omega_\mathrm{Q}) \right\}. \tag{4.3}$$

For both domains, we choose the test functions to come from the same space as the trial functions. Let $(\phi, \psi) \in \mathcal{W}_\mathrm{G}$ be test functions for (P, T_G), and let $\zeta \in \mathcal{W}_\mathrm{Q}$ be the test function for T_Q. We derive the variational form of the thermoacoustic equations (2.13) by multiplying (2.13a) by ϕ, multiplying (2.13b) by ψ, integrating over Ω_G, and performing standard integration by parts. We perform a similar procedure for the heat equation (2.9). Using the boundary conditions and the continuity conditions (2.10), the variational problem becomes that of finding $(P, T_G) \in \mathcal{W}_\mathrm{G}$ and $T_Q \in \mathcal{W}_\mathrm{Q}$ such that

$$-\xi\langle \mathbf{B}(\mathbf{x})\nabla P, \nabla\phi\rangle + a_1\langle \beta_x\beta_z P, \phi\rangle + a_2\langle \beta_x\beta_z T_G, \phi\rangle = ia_3\langle S, \phi\rangle, \tag{4.4a}$$

$$-\kappa\langle \mathbf{B}(\mathbf{x})\nabla T_G, \nabla\psi\rangle - ib_1\langle \beta_x\beta_z P, \psi\rangle + ib_2\langle \beta_x\beta_z T_G, \psi\rangle = -\langle S, \psi\rangle - \int_{\Gamma_\mathrm{I}} \left[(\boldsymbol{\kappa_Q}\nabla T_Q)\cdot\mathbf{n}\right]\psi\, ds, \tag{4.4b}$$

$$-\langle \boldsymbol{\kappa_Q}\nabla T_Q, \nabla\zeta\rangle + ic_1\langle T_Q, \zeta\rangle = -\kappa\int_{\Gamma_\mathrm{I}} (\nabla T_G\cdot\mathbf{n})\,\zeta\, ds \tag{4.4c}$$

for all $(\phi, \psi) \in \mathcal{W}_\mathrm{G}$ and $\zeta \in \mathcal{W}_\mathrm{Q}$. Here the notation $\langle\cdot\,,\cdot\rangle$ represents the standard L^2 inner product for complex functions. The variational formulation leads to a linear

system $\mathbf{Au} = \mathbf{b}$, where

$$\mathbf{A} = \left[\begin{array}{cc|c} a_1\mathbf{M} - \xi\mathbf{K} & a_2\mathbf{M} & \mathbf{0} \\ -ib_1\mathbf{M} & ib_2\mathbf{M} - \kappa\mathbf{K} & \mathbf{N}_{\mathrm{Q}\to\mathrm{G}} \\ \hline \mathbf{0} & \mathbf{N}_{\mathrm{G}\to\mathrm{Q}} & ic_1\mathbf{M}_{\mathrm{Q}} - \mathbf{K}_{\mathrm{Q}} \end{array}\right],$$

$$\mathbf{u} = \begin{bmatrix} \overrightarrow{\mathbf{P}} \\ \overrightarrow{\mathbf{T}}_{\mathrm{G}} \\ \overrightarrow{\mathbf{T}}_{\mathrm{Q}} \end{bmatrix}, \quad \mathbf{b} = \begin{bmatrix} ia_3\overrightarrow{\mathbf{S}}_{\mathrm{P}} \\ -\overrightarrow{\mathbf{S}}_{\mathrm{T}} \\ \mathbf{0} \end{bmatrix}, \tag{4.5}$$

with stiffness matrices, mass matrices, and load vectors defined by

$$\begin{aligned} \mathbf{K}_{ij} &= \int_{\Omega_{\mathrm{G}}} \nabla\phi_i(\mathbf{x})^{\mathrm{T}}\mathbf{B}(\mathbf{x})\nabla\phi_j(\mathbf{x})\,d\mathbf{x}, & \mathbf{M}_{ij} &= \int_{\Omega_{\mathrm{G}}} \beta_x\beta_z\phi_i(\mathbf{x})\phi_j(\mathbf{x})\,d\mathbf{x}, \\ (\mathbf{K}_{\mathrm{Q}})_{ij} &= \int_{\Omega_{\mathrm{Q}}} \nabla\xi_i(\mathbf{x})^{\mathrm{T}}\boldsymbol{\kappa_Q}\nabla\xi_j(\mathbf{x})\,d\mathbf{x}, & (\mathbf{M}_{\mathrm{Q}})_{ij} &= \int_{\Omega_{\mathrm{Q}}} \xi_i(\mathbf{x})\xi_j(\mathbf{x})\,d\mathbf{x}, \\ (\overrightarrow{\mathbf{S}}_{\mathrm{P}})_i &= \int_{\Omega_{\mathrm{G}}} \phi_i(\mathbf{x})S(\mathbf{x})\,d\mathbf{x}, & (\overrightarrow{\mathbf{S}}_{\mathrm{T}})_i &= \int_{\Omega_{\mathrm{G}}} \psi_i(\mathbf{x})S(\mathbf{x})\,d\mathbf{x}. \end{aligned} \tag{4.6}$$

The interfacial matrices, $\mathbf{N}$, represent couplings between T_G and T_Q:

$$(\mathbf{N}_{\mathrm{Q}\to\mathrm{G}})_{ij} = \int_{\Gamma_{\mathrm{I}}} \left[(\boldsymbol{\kappa_Q}\nabla\zeta_j(\mathbf{x}))\cdot\mathbf{n}\right]\psi_i(\mathbf{x})\,ds, \tag{4.7a}$$

$$(\mathbf{N}_{\mathrm{G}\to\mathrm{Q}})_{ij} = \kappa\int_{\Gamma_{\mathrm{I}}} \left[\nabla\psi_j(\mathbf{x})\cdot\mathbf{n}\right]\zeta_i(\mathbf{x})\,ds. \tag{4.7b}$$

Since we need to adequately resolve both the laser and the air-QTF interface, the size of the problem is often large. Thus, if we are to solve the linear system (4.5) using the GMRES algorithm [52], an efficient preconditioning scheme is essential. A partial motivation for our approach is due to the recent work by Brennan and Kirby [9], who tested a variety of preconditioners including block Jacobi and block Gauss–Seidel preconditioners for the thermoacoustic equations (2.5) on a rectangular domain. To solve the linear system (4.5), we use Brennan's block Gauss–Seidel preconditioner with an extension that corresponds to the heat equation in the QTF, given by

$$\mathbf{P}_{\mathrm{global}} = \begin{bmatrix} a_1\mathbf{M} - \xi\mathbf{K} & 0 & 0 \\ -ib_1\mathbf{M} & ib_2\mathbf{M} - \kappa\mathbf{K} & 0 \\ 0 & \mathbf{N}_{\mathrm{G}\to\mathrm{Q}} & ic_1\mathbf{M}_{\mathrm{Q}} - \mathbf{K}_{\mathrm{Q}} \end{bmatrix}. \tag{4.8}$$

The action of the preconditioner requires solving the diagonal blocks in (4.8). In particular, implementation of the PML method adds significant challenges to inverting the first two diagonal blocks. For the pressure block $\mathbf{H}_{\mathrm{P}} := a_1\mathbf{M} - \xi\mathbf{K}$ and the temperature block $\mathbf{H}_{\mathrm{T}} := ib_2\mathbf{M} - \kappa\mathbf{K}$, we use the custom preconditioner from section 3, as formulated in Algorithm 1. Finally, we solve the block that corresponds to the heat equation in the QTF using the GMRES algorithm preconditioned with the AMG method. In Algorithm 2, we assemble the pieces together to form the action of the preconditioner on $\mathbf{b}^{\mathrm{T}} = [\mathbf{b}_P^{\mathrm{T}}\ \mathbf{b}_{T_G}^{\mathrm{T}}\ \mathbf{b}_{T_Q}^{\mathrm{T}}]$.

5. Numerical results. In this section, we present our numerical results both for the performance of the custom preconditioner (3.16) and the solution of the thermoacoustic system (4.5). The computational results shown here were obtained on the

Algorithm 2 Global preconditioner (4.8): $\mathbf{u} \leftarrow \mathbf{P}_{\text{global}}^{-1}\mathbf{b}$, with $\mathbf{b}^{\mathrm{T}} = [\mathbf{b}_P^{\mathrm{T}}\ \mathbf{b}_{T_G}^{\mathrm{T}}\ \mathbf{b}_{T_Q}^{\mathrm{T}}]$

1: Initialize auxiliary vector $\mathbf{z}_{T_G}$ and $\mathbf{z}_{T_Q}$ of the same size as $\mathbf{b}_{T_A}$ and $\mathbf{b}_{T_Q}$, respectively
2: Approximate $\mathbf{p} \approx \mathbf{H}_{\mathrm{P}}^{-1}\mathbf{b}_P$ using Algorithm 1 implemented for pressure
3: Block-eliminate pressure: $\mathbf{z}_{T_G} = \mathbf{b}_{T_G} + ib_1\mathbf{M}\mathbf{p}$
4: Approximate $\boldsymbol{\tau} \approx \mathbf{H}_{\mathrm{T}}^{-1}\mathbf{z}_{T_G}$ using Algorithm 1 implemented for temperature
5: Determine $\mathbf{z}_{T_Q} = \mathbf{b}_{T_Q} - \mathbf{N}_{G\to Q}\boldsymbol{\tau}$
6: Solve $(ic_1\mathbf{M}_{\mathrm{Q}} - \mathbf{K}_{\mathrm{Q}})\boldsymbol{\tau}_Q = \mathbf{z}_{T_Q}$ with GMRES preconditioned by AMG
7: Return $\mathbf{u} = \begin{bmatrix} \mathbf{p} \\ \boldsymbol{\tau}_G \\ \boldsymbol{\tau}_Q \end{bmatrix}$

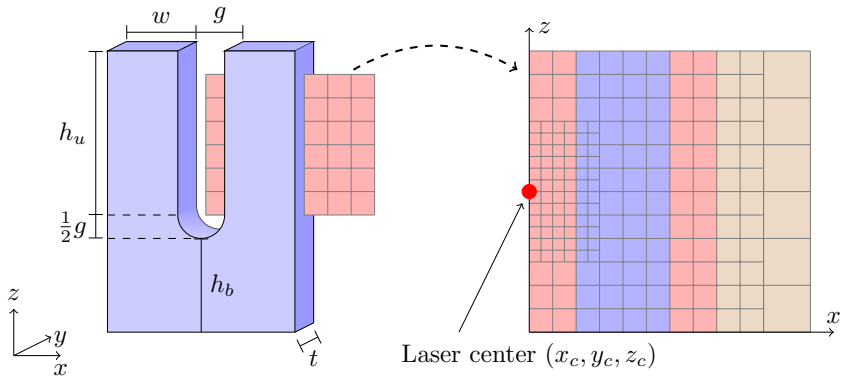

FIG. 4. *Left: Geometry of the QTF. Right: Visualization of our adaptive refinement strategy of a 2D slice passing through the tuning fork, as shown on the left. The QTF domain is shown in blue, the gas in pink, and the PML in brown. Color is available online only.*

Stampede 1 cluster at the Texas Advanced Computing Center at the University of Texas at Austin.

The finite element matrices were assembled using the `deal.II` package [7]. The mesh was generated using the `Gmsh` package [25], and automatic mesh partitioning for the parallel computation was done using `p4est` [11]. As complex numbers are not yet fully supported within `deal.II`, we decompose the variables into real and imaginary components and assemble the real system by using the distributed matrices and vectors available in the `Trilinos` package [29]. We then convert the real matrices and vectors to their complex version, stored as `PETSc` objects [5, 6]. For the sparse parallel LU solver, we use `MUMPS` [2, 3]. In order to reduce the number of unknowns, we use adaptive refinement as shown in Figure 4(right), available in the `deal.II` package. In particular, we perform multiple refinements near the laser in order to resolve the beam accurately. We also use a coarse mesh in the PML region to reduce the size of the PML problem for the LU solver.

The geometry of the tuning fork is shown in Figure 4(left), and the parameters describing the tuning fork are listed in Table 1. We assume that the experiment is conducted in nitrogen gas (N_2), although other choices are also possible [19, 46, 49]. The parameter values for the laser source are given in Table 2. (Values in Tables 1

TABLE 1
QTF parameters: $C_{p,Q}$ (specific heat capacity), ρ_Q (density), κ_j (coefficients of the thermal conductivity tensor), w (tine width), g (gap between the tines), h_u (height of the tine), h_b (height of the QTF from the bottom up to the gap), and t (tine thickness).

Constant	Value	Units
$C_{p,Q}$	733	J/(kg·K)
ρ_Q	2650	kg/m^3
κ_1	6.5	W/(m·K)
κ_2	6.5	W/(m·K)
κ_3	11.3	W/(m·K)

Constant	Value [mm]
w	0.6
g	0.3
h_u	3.75
h_b	2.33
t	0.34

TABLE 2
Laser source parameters for an experimental setup with nitrogen gas.

Constant	Interpretation	Value	Units
ω	Angular frequency of laser	$2.061 \cdot 10^5$	rad/s
α_{eff}	Absorption coefficient of N_2	0.05	1/m
W_L	Laser power	$3 \cdot 10^{-2}$	W
σ	Beam waist	$7.5 \cdot 10^{-6}$	m
y_R	Rayleigh length $\pi\sigma^2/\lambda$	$1.126 \cdot 10^{-4}$	m

and 2 are taken from Petra et al. [49]). We implemented our code to support simulations of experiments in which the ambient pressure ranges from 5 to 800 Torr (760 Torr = 1 atm). For our numerical simulations, we chose parameters that correspond to QEPAS and ROTADE sensors (see Table 3).

5.1. Preconditioner for the scalar Helmholtz equation with PML. We first study the characteristics of our custom preconditioner (3.16) for a finite element discretization of the scalar Helmholtz problem with PML given in (3.1). We scale our problem to a unit domain, which yields a wavenumber of $k \approx 0.5$. However, this small wavenumber affects the implementation of PML. The "rule of thumb" approach to modeling PML regions is to make the width of the domain approximately half a wavelength [13] and to use a relatively small attenuation coefficient, A, in (2.12). However, these choices of parameters are not practical since the wavelength corresponding to our problem, $\ell = 2\pi/k \approx 4\pi$, would generate too wide of a PML region. Instead we opt for a thin PML region and relatively large attenuation coefficients. Specifically, we chose a PML layer of thickness 0.16 with $A = 400\omega$. The trade-off with this approach, however, is that the resulting problem is more indefinite.

We begin by testing our approach on the pressure block $\mathbf{H}$ with the right-hand side being the scaled laser source term given in (2.2). In Figure 5, we compare the spectrum of the unpreconditioned (left) and the preconditioned (right) operators for the Helmholtz equation with PML for a problem with 4489 degrees of freedom (DoFs). The result in Figure 5(right) shows that the eigenvalues of the preconditioned matrix are clustered near one and indicates that the eigenspectrum is no longer indefinite. We also find that the number of nonunitary eigenvalues for the preconditioned operator is equal to 200, which agrees with the statement of Theorem 3.1, as the size of the interface $\mathcal{V}_\mathcal{I}$ for this problem is also 200.

We now turn to the performance of the preconditioner. In the 2D case, the strong scaling plot in Figure 6(left) demonstrates that the preconditioner parallelizes fairly well. In particular, the scalability of the LU subsolver was not a significant issue

TABLE 3

Constants for the thermoacoustic experiments using N_2 gas for both the ROTADE and the QEPAS parameter regimes. References are given in the rightmost column.

Constant	Interpretation	ROTADE	QEPAS	Units	
T_0	Ambient temperature	20	20	°C	[48], [49]
P_0	Ambient pressure	5	450	Torr	
κ	Thermal conductivity of N_2	0.0254	0.0254	W/(m·K)	
ρ	Density of N_2	0.007662	0.6898	kg/m^3	
C_p	Specific heat capacity of N_2	1039.7	1039.7	J/(kg·K)	
μ	Shear viscosity	$1.785 \cdot 10^{-5}$	$1.785 \cdot 10^{-5}$	kg/(m·s)	[16]
η	Bulk viscosity	$1.317 \cdot 10^{-5}$	$1.317 \cdot 10^{-5}$	kg/(m·s)	[15]
γ	Isentropic expansion factor of diatomic gas	7/5	7/5	none	[42]
c	Speed of sound in N_2	348.7	348.7	m/s	
α	$\partial P/\partial T$ under constant volume	2.274	204.656	Pa/K	
ℓ_h	Characteristic length of conductivity	$9.124 \cdot 10^{-6}$	$1.013 \cdot 10^{-7}$	m	
ℓ_v	Characteristic length of viscosity	$1.383 \cdot 10^{-5}$	$1.5347 \cdot 10^{-7}$	m	

due to the relatively small problem size in the PML region. In Figure 6(right), we show the outer GMRES residuals of the preconditioned iterations as a function of problem size. The plots follow nearly the same profile regardless of the size of the problem, suggesting that for the Helmholtz problem with PML there exists a mesh-independent bound for the rate of convergence of the preconditioner with respect to problem size. This idea is further supported by Table 4, where we show how the extreme eigenvalues and the condition number of the preconditioned system depend on the number of DoFs, compared to the condition number of the unpreconditioned system. The results demonstrate that these quantities remain fairly uniform for the preconditioned system as problem size increases.

Both Krylov subspace solvers in Algorithm 1 cost $\mathcal{O}(Nk)$, where N is the global size of the linear system, and k is the number of iterations required to solve the particular problem. Since our numerical experiments show that the number of iterations for all the Krylov solvers remains nearly fixed as the problem size increases, we can treat k as constant and therefore conclude that both CG and GMRES solve their corresponding problems at a cost of $\mathcal{O}(N)$. However, the direct solver does not scale linearly, as the cost of factorization is $\mathcal{O}(N_{\text{PML}}^2)$ [39], where N_{PML} is the size of the problem in the PML region. Therefore, for the results in this paper, we chose to minimize the computational footprint of the LU solver by using a coarse initial mesh and refining only in the computational domain, not in the PML region, where the direct solver is used. In our simulations, this approach worked well since the PML parameters were chosen so that the PML adequately damps reflections even with the coarse mesh. In Table 5, we show a comparison between the global problem size and the number of unknowns in the PML region. The results in the table demonstrate that the size of the PML region grows at a rate proportional to the square root of the global problem size.

Finally, we study the behavior of the preconditioner for the Helmholtz problem with PML for higher frequency cases. In order to focus solely on the performance of the

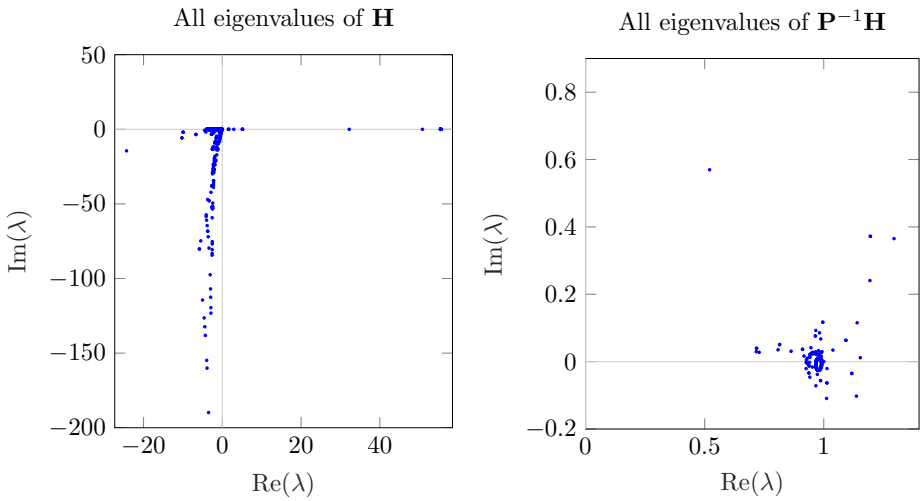

FIG. 5. *Left: Eigenvalues of the unpreconditioned block* $\mathbf{H}$. *Right: Spectrum of the preconditioned system* $\mathbf{P}^{-1}\mathbf{H}$. *Problem size:* 4489 *DoFs.*

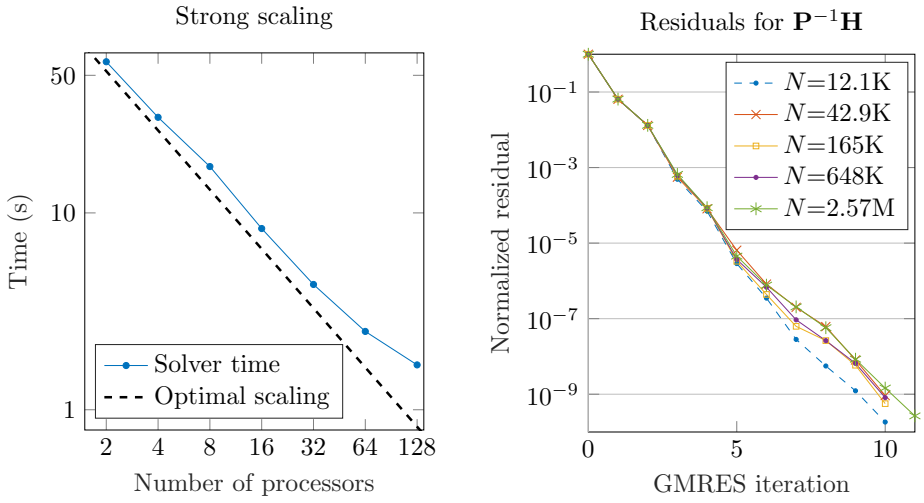

FIG. 6. *Left: Strong scaling for the custom preconditioner (*2.57 *million DoFs). Right: Normalized residuals of the preconditioned GMRES iterations as a function of problem size* N.

preconditioner, we use exact solvers for all the inner blocks. In Table 6, we show the number of outer GMRES iterations and the extreme eigenvalues of the preconditioned operator for different values of wavenumber k. Further numerical testing using the SLEPc package [28] shows that the preconditioned system does not have eigenvalues with a negative real part up to wavenumbers of $k = 300$. As is evident from the table, the largest eigenvalue is nearly 1 regardless of the problem size, while the smallest eigenvalue gradually tends to zero. This is the expected behavior since all Helmholtz problems become more indefinite as k increases.

5.2. Results for the thermoacoustic equations. In this section, we discuss the numerical solution of the thermoacoustic equations in three dimensions.

TABLE 4
Smallest and largest eigenvalues, and the condition number of the preconditioned scalar Helmholtz operator with PML in two dimensions as a function of the number of DoFs. The last column shows the condition number for the unpreconditioned operator.

DoF count	$\lambda_{\min}(\mathbf{P}^{-1}\mathbf{H})$	$\lambda_{\max}(\mathbf{P}^{-1}\mathbf{H})$	$\kappa(\mathbf{P}^{-1}\mathbf{H})$	$\kappa(\mathbf{H})$
4.49K	$0.717 + 0.029i$	$1.295 + 0.365i$	2.085	$2.19 \cdot 10^5$
12.1K	$0.479 + 0.021i$	≈ 1	2.335	$7.33 \cdot 10^5$
42.9K	$0.475 + 0.018i$	≈ 1	2.676	$2.83 \cdot 10^6$
165K	$0.472 + 0.015i$	≈ 1	2.896	$1.12 \cdot 10^7$
648K	$0.467 + 0.016i$	$0.996 + 0.226i$	3.466	$4.46 \cdot 10^7$

TABLE 5
The number of unknowns in the PML region as a function of global problem size.

Problem size n	12089	42905	164521	647737	2574153
PML region size	1888	2504	3720	6136	10952

We discuss the validation of the computational solution to the thermoacoustic equations (2.13) and scalability results in supplementary section SM2. Here we focus our attention on the full computational problem, namely the solution of the thermoacoustic equations with PML in the air coupled to thermal dissipation in the QTF. We solve the resulting linear system given in (4.5) using GMRES with the block Gauss–Seidel preconditioner in (4.8). To put the numerical solutions into context, we find it useful to compare them to the following:

1. Solutions obtained by modeling only the thermal (ROTADE) or the acoustic (QEPAS) component of the process. In supplementary section SM3, we show how the equations for the simplified models can be obtained from the thermoacoustic equations under certain additional assumptions.
2. The free-space solution described in supplementary section SM1 in the absence of a QTF. This comparison enables us to describe exactly how the presence of the QTF affects the thermoacoustic wave.

In the following discussion, we define the origin of the coordinate system to be at the bottom of the gap between the tines and halfway between the front and back faces of the tuning fork (see Figure 4).

We first present our results for the ROTADE parameter regime. To obtain optimal sensitivity for a ROTADE sensor, the laser beam should be located near the bottom of the gap between the tines. As in Petra et al. [49], we chose the axis of the laser beam to pass through the center of the semicylinder of the tuning fork located at $(x_s, z_s) = (0, g/2)$. Since the solutions are symmetric about the plane $x = 0$, we only plot them in the region $x \geq 0$. In Figure 7, we show x slices of the amplitude of the temperature. The thick blue line is the temperature component of the numerical solution of the thermoacoustic equations. The thin red line corresponds to the solution of the heat equation only, and the dashed black line is the analytical solution. In the regions near the laser source and interior to the tuning fork, the solution of the heat equation agrees closely with the solution to the thermoacoustic equations. The agreement between the temperature solution of the thermoacoustic equations and the solution to the classical heat equation at the interface between the QTF and the air provides a validation for the use of the heat equation in the previous computational model of a ROTADE sensor by Petra et al. [49]. However, outside the QTF the

TABLE 6

Number of outer GMRES iterations for the preconditioner for the scalar Helmholtz problem with PML for different values of the wavenumber k. In order to resolve the high-energy modes, computations for the higher-frequency problems were done on finer meshes.

k	Outer iteration count	$\lambda_{\min}(\mathbf{P}^{-1}\mathbf{H})$	$\lambda_{\max}(\mathbf{P}^{-1}\mathbf{H})$
5	7	$0.331 + 0.151i$	$1 + 0.349i$
10	9	$0.329 + 0.044i$	$1.01 - 0.039i$
20	11	$0.237 + 0.172i$	≈ 1
40	14	$0.210 + 0.111i$	≈ 1
60	17	$0.202 + 0.087i$	≈ 1
80	17	$0.191 + 0.067i$	≈ 1
100	18	$0.185 + 0.048i$	≈ 1
200	21	$0.137 + 0.048i$	≈ 1

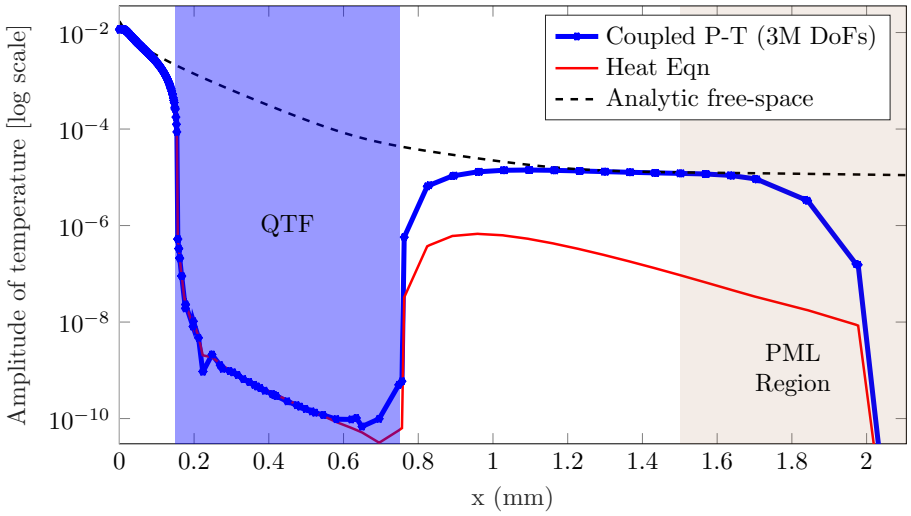

FIG. 7. *x-slices (for $x \geq x_s$) of the temperature for three different models. The laser is centered at $x_s = 0$ mm. The white space represents the trace gas, and blue is the tuning fork. Color is available online only.*

solution of the thermoacoustic equations decays significantly less rapidly than does the heat equation solution due to the relationship between the temperature and pressure established in supplementary section SM1. On the QTF interface near the laser source, the amplitude of the temperature given by the simulations is nearly 4×10^4 smaller than that given by the free-space analytical solution due to the rapid heat dissipation into the QTF. Nonetheless, we observe that the analytic free-space solution agrees closely with the solution of the thermoacoustic equations at a sufficient distance from the QTF. The far-field agreement between the two models can be attributed to the fact that the size of the QTF is much smaller than the wavelength of the laser source.

In Figure 8(left), we compare slices of the amplitude of the pressure obtained by solving the thermoacoustic equations (shown as a thick blue line) to those obtained by solving the wave equation (thin red line), both with ROTADE parameters. In the gap between the tines, the amplitude of the solution to the wave equation is nearly double that of the thermoacoustic equations. This difference is also present in the

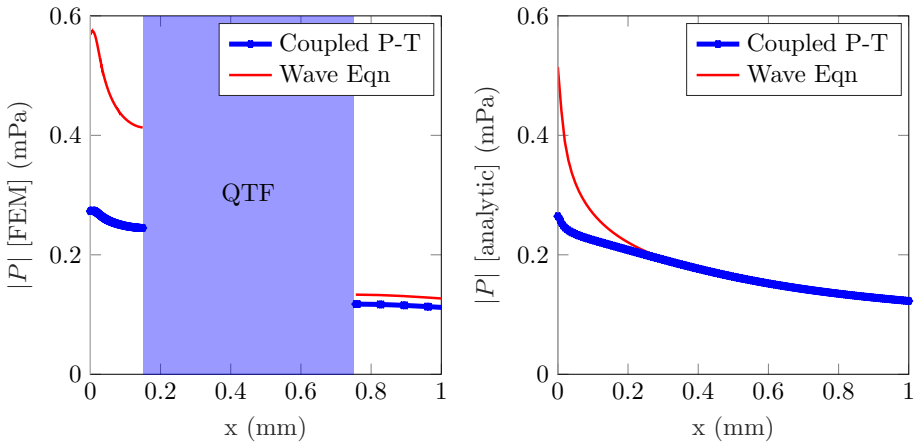

FIG. 8. *Comparison of solutions obtained using the thermoacoustic equations and the classical wave equation with ROTADE parameters. Left: Computational solutions obtained by solving the equations in the presence of a QTF. Right: Analytic free-space solutions obtained from solving the two equations.*

analytic solutions without a QTF, as can be observed in Figure 8(right), where we show slices of the amplitude of the pressure in free space. The thick blue line is the analytic free-space solution to the thermoacoustic equations, and the thin red line is the analytic solution to the wave equation. Both plots in Figure 8 show that for the ROTADE parameter set, the pressure solution of the thermoacoustic equations is significantly different from that of the acoustic wave equation.

In Figure 9, we show the results for the amplitude (left) and phase (right) of the acoustic pressure for the QEPAS parameters given in Table 3. For these simulations, the laser was focused near the top of the tines of the tuning fork, centered at $(x_s, z_s) = (0, h_u)$. Since heat dissipates much more rapidly in the QEPAS regime, the thermal wave is negligible at the surface of the QTF. Therefore, the acoustic signal dominates, and the pressure component of the thermoacoustic equations is nearly identical to the solution to the wave equation (not shown in the figure). On the other hand, the difference between the profiles of the analytical and the numerical solutions suggests an explanation for a discrepancy in [48]. In that paper, Petra et al. approximated the pressure wave in the exterior of the QTF by analytically solving the free-space wave equation with the laser source. They then estimated the force that acts upon the tuning fork due to the acoustic wave by computing the difference in pressure values on the inner and outer faces of the tines. Based on these approximations, Petra et al. computed the electric current generated by the QTF. However, their results were about two times smaller than the signal obtained from experimental measurements. In our case, the force on the tuning fork obtained using the thermoacoustic model is approximately 2.4 times larger than that obtained using the analytical free-space solution. By the linearity of the process, the recovered signal would also be multiplied by the same amount and thus would agree much more closely with the experimental data.

Finally, we describe a situation in which the coupling in the pressure-temperature equations significantly alters the pressure solution relative to the solution of the acoustic wave equation alone. For this simulation, we used the ROTADE parameters but centered the laser closer to one of the tines at $(x_s, z_s) = (g/4, h_u/2)$. This choice

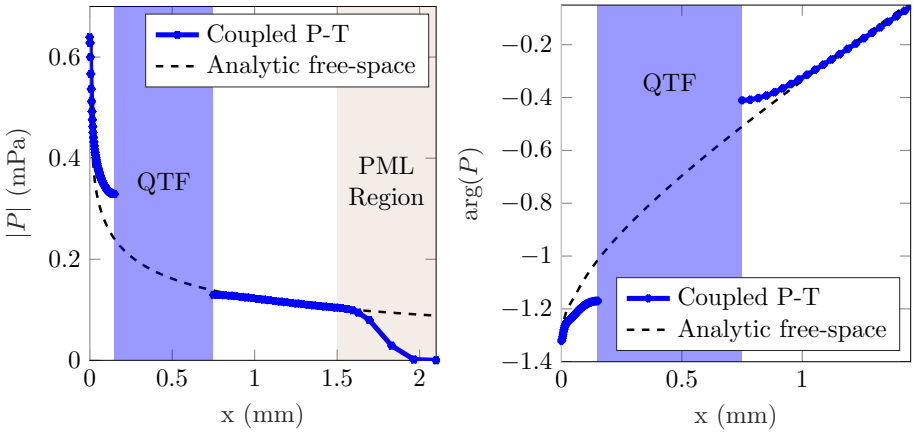

FIG. 9. *Plots of x-slices (for $x \geq x_s$) for the pressure obtained with QEPAS parameters. Left: Comparison between the amplitude of the pressure for the numerical solution to the thermoacoustic equation and the free-space solution to the coupled pressure-temperature equations. Right: Comparison between the phase of the thermoacoustic pressure solution obtained computationally and analytically.*

of laser position is within the region where Kosterev and Doty [33] observed poor sensitivity of the sensor. In Figure 10, we show that the pressure obtained by solving the thermoacoustic equations predicts a smaller net force on the QTF than that obtained from the wave equation. The primary reason for this difference is that in the ROTADE parameter regime, the temperature acts as a source in the thermoacoustic pressure equation (2.6a). Moreover, because of the thermal diffusion in (2.6b), this temperature source has a lower amplitude and is wider than the source function, S, in the supplementary acoustic wave equation (SM3.4). This interaction between the temperature and pressure waves is one of the factors that influences the sensitivity of the sensor in this parameter regime.

6. Conclusions. We have developed and implemented a computational method for solving the thermoacoustic equations in gas coupled with thermal dissipation in a QTF for the purpose of more accurate modeling of trace gas sensors. To obtain the solutions in an efficient manner, we implemented a block preconditioning scheme, with a custom preconditioner for the scalar Helmholtz equation with PML. Our numerical simulations demonstrate that our approach is valid for modeling both QEPAS and ROTADE sensors. Our results also suggest reasons for an experimental phenomenon observed in Kosterev and Doty [33] and for a discrepancy between numerical and experimental models in Petra et al. [48], which have not previously been explained. Finally, the numerical studies indicate that the preconditioner we derived for the Helmholtz problem with PML is both scalable and mesh-independent.

The next phase of our modeling will include coupling to the thermoelastic displacement of the tuning fork. In particular, we intend to model the damping of the tuning fork as it moves through the viscous fluid by incorporating the viscous stress tensor of the fluid into conditions on the interface between the air and the tuning fork. In addition, we intend to use the thermoacoustic equations in a model for a QEPAS sensor in which boundary layer effects may occur due to the close proximity between the tuning fork and the surface of a microresonator tube [18]. We note that recent interest in further miniaturization of QEPAS sensors [26] means the modeling

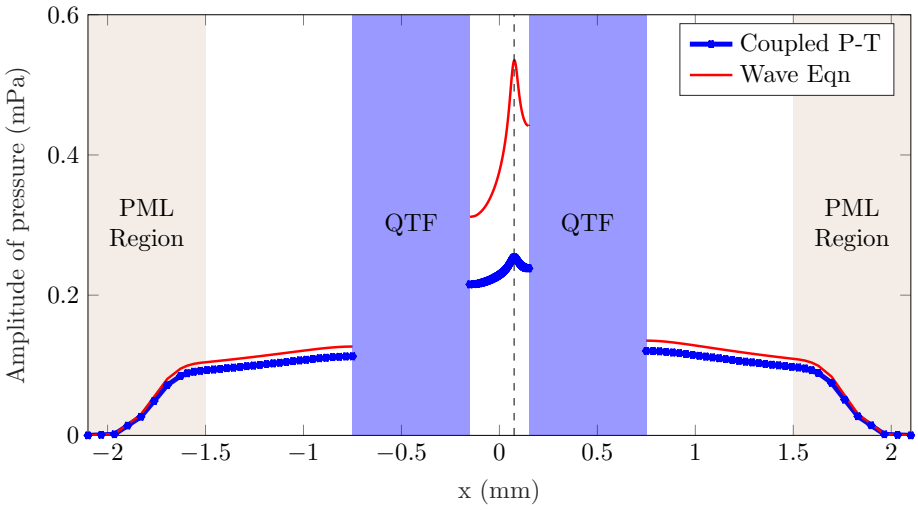

FIG. 10. *A comparison of pressure solutions for ROTADE parameters, with the laser beam focused halfway up the gap between the tines and off-center at* $x_s = g/4$ *(vertical dashed line).*

of thermal and viscous boundary layers becomes more significant, emphasizing the importance of our model.

Acknowledgments. We thank Brian Brennan, Robert Kirby (Baylor University), Matthew Knepley (Rice University), Anatoliy Kosterev (Yokogawa Corp.), Noemi Petra (University of California, Merced), and the `deal.II` and `PETSc` communities for helpful discussions. We also thank the referees for their insightful comments.

REFERENCES

[1] M. ADAMS, *Algebraic multigrid methods for direct frequency response analyses in solid mechanics*, Comput. Mech., 39 (2007), pp. 497–507.

[2] P. R. AMESTOY, I. S. DUFF, J.-Y. L'EXCELLENT, AND J. KOSTER, *A fully asynchronous multifrontal solver using distributed dynamic scheduling*, SIAM J. Matrix Anal. Appl., 23 (2001), pp. 15–41, https://doi.org/10.1137/S0895479899358194.

[3] P. R. AMESTOY, A. GUERMOUCHE, J.-Y. L'EXCELLENT, AND S. PRALET, *Hybrid scheduling for the parallel solution of linear systems*, Parallel Comput., 32 (2006), pp. 136–156.

[4] G. AOUST, R. LEVY, B. BOURGETEAU, AND O. L. TRAON, *Viscous damping on flexural mechanical resonators*, Sens. Actuator A-Phys., 230 (2015), pp. 126–135.

[5] S. BALAY, S. ABHYANKAR, M. F. ADAMS, J. BROWN, P. BRUNE, K. BUSCHELMAN, L. DALCIN, V. EIJKHOUT, W. D. GROPP, D. KAUSHIK, M. G. KNEPLEY, L. C. MCINNES, K. RUPP, B. F. SMITH, S. ZAMPINI, H. ZHANG, AND H. ZHANG, `PETSc` *Users Manual*, Technical report ANL-95/11: Revision 3.7, Argonne National Laboratory, Lemont, IL, 2016.

[6] S. BALAY, W. D. GROPP, L. C. MCINNES, AND B. F. SMITH, *Efficient management of parallelism in object oriented numerical software libraries*, in Modern Software Tools in Scientific Computing, E. Arge, A. M. Bruaset, and H. P. Langtangen, eds., Birkhäuser, Basel, 1997, pp. 163–202.

[7] W. BANGERTH, R. HARTMANN, AND G. KANSCHAT, `deal.II`*—a general purpose object oriented finite element library*, ACM Trans. Math. Software, 33 (2007), 24.

[8] J.-P. BERENGER, *A perfectly matched layer for the absorption of electromagnetic waves*, J. Comput. Phys., 114 (1994), pp. 185–200.

[9] B. BRENNAN AND R. C. KIRBY, *Finite element approximation and preconditioners for a coupled thermal-acoustic model*, Comput. Math. Appl., 70 (2015), pp. 2342–2354.

[10] B. BRENNAN, R. C. KIRBY, J. ZWECK, AND S. E. MINKOFF, *High-performance python-based simulations of pressure and temperature waves in a trace gas sensor*, in Proceedings of

PyHPC 2013: Python for High Perfomance and Scientific Computing, 2013.
[11] C. Burstedde, L. C. Wilcox, and O. Ghattas, `p4est:` *Scalable algorithms for parallel adaptive mesh refinement on forests of octrees*, SIAM J. Sci. Comput., 33 (2011), pp. 1103–1133, https://doi.org/10.1137/100791634.
[12] Y. Cao and G. J. Diebold, *Effects of heat conduction and viscosity on photoacoustic waves from droplets*, Opt. Eng., 36 (1997), pp. 417–422.
[13] Z. Chen, D. Cheng, W. Feng, T. Wu, and H. Yang, *A multigrid-based preconditioned Krylov subspace method for the Helmholtz equation with PML*, J. Math. Anal. Appl., 383 (2011), pp. 522–540.
[14] W. C. Chew and W. H. Weedon, *A 3D perfectly matched medium from modified Maxwell's equations with stretched coordinates*, Microw. Opt. Technol. Lett., 7 (1994), pp. 599–604.
[15] M. S. Cramer, *Numerical estimates for the bulk viscosity of ideal gases*, Phys. Fluids, 24 (2012), 066102.
[16] Crane Co., *Flow of Fluids Through Valves, Fittings, and Pipe*, Technical paper 410, Crane Co., New York, 1982.
[17] R. Curl, F. Capasso, C. Gmachl, A. Kosterev, B. McManus, R. Lewicki, M. Pusharsky, G. Wysocki, and F. Tittel, *Quantum cascade lasers in chemical physics*, Chem. Phys. Lett., 487 (2010), pp. 1–18.
[18] L. Dong, A. A. Kosterev, D. Thomazy, and F. K. Tittel, *QEPAS spectrophones: Design, optimization, and performance*, Appl. Phys. B, 100 (2010), pp. 627–635.
[19] A. Elia, P. M. Lugará, C. Di Franco, and V. Spagnolo, *Photoacoustic techniques for trace gas sensing based on semiconductor laser sources*, Sensors, 9 (2009), pp. 9616–9628.
[20] B. Engquist and L. Ying, *Sweeping preconditioner for the Helmholtz equation: Moving perfectly matched layers*, Multiscale Model. Simul., 9 (2011), pp. 686–710, https://doi.org/10.1137/100804644.
[21] Y. A. Erlangga, *Advances in iterative methods and preconditioners for the Helmholtz equation*, Arch. Comput. Methods Eng., 15 (2008), pp. 37–66.
[22] Y. A. Erlangga, C. W. Oosterlee, and C. Vuik, *A novel multigrid based preconditioner for heterogeneous Helmholtz problems*, SIAM J. Sci. Comput., 27 (2006), pp. 1471–1492, https://doi.org/10.1137/040615195.
[23] S. Firebaugh, E. Terray, and L. Dong, *Optimization of Resonator Radial Dimensions for Quartz Enhanced Photoacoustic Spectroscopy Systems*, Proc. SPIE 8600, 2013.
[24] S. L. Firebaugh, A. Sampaolo, P. Patimisco, V. Spagnolo, and F. K. Tittel, *Modeling the dependence of fork geometry on the performance of quartz enhanced photoacoustic spectroscopic sensors*, in Proceedings of the 2015 IEEE Conference on Lasers and Electro-Optics (CLEO), 2015, ATu1J3.
[25] C. Geuzaine and J.-F. Remacle, `Gmsh:` *A 3-D finite element mesh generator with built-in pre- and post-processing facilities*, Internat. J. Numer. Methods Engrg., 79 (2009), pp. 1309–1331.
[26] A. Glière, J. Rouxel, B. Parvitte, S. Boutami, and V. Zéninari, *A coupled model for the simulation of miniaturized and integrated photoacoustic gas detector*, Int. J. Thermophys., 34 (2013), pp. 2119–2135.
[27] F. J. Harren, J. Mandon, and S. M. Cristescu, *Photoacoustic spectroscopy in trace gas monitoring*, in Encyclopedia of Analytical Chemistry, John Wiley & Sons, Chichester, UK, 2000, pp. 2203–2226.
[28] V. Hernandez, J. E. Roman, and V. Vidal, *SLEPc: A scalable and flexible toolkit for the solution of eigenvalue problems*, ACM Trans. Math. Software, 31 (2005), pp. 351–362.
[29] M. Heroux, R. Bartlett, V. H. R. Hoekstra, J. Hu, T. Kolda, R. Lehoucq, K. Long, R. Pawlowski, E. Phipps, A. Salinger, H. Thornquist, R. Tuminaro, J. Willenbring, and A. Williams, *An Overview of Trilinos*, Technical report SAND2003-2927, Sandia National Laboratories, Albuquerque, NM, 2003.
[30] J. Kaderli, J. Zweck, A. Safin, and S. Minkoff, *An analytic solution to the coupled pressure-temperature equations for modeling of photoacoustic trace gas sensors*, J. Engrg. Math., 103 (2017), pp. 173–193.
[31] G. A. A. Kahou, E. Kamgnia, and B. Philippe, *An explicit formulation of the multiplicative Schwarz preconditioner*, Appl. Numer. Math., 57 (2007), pp. 1197–1213.
[32] A. Kosterev, Y. Bakhirkin, R. Curl, and F. Tittel, *Quartz-enhanced photoacoustic spectroscopy*, Opt. Lett., 27 (2002), pp. 1902–1904.
[33] A. A. Kosterev and J. H. Doty III, *Resonant optothermoacoustic detection: Technique for measuring weak optical absorption by gases and micro-objects*, Opt. Lett., 35 (2010), pp. 3571–3573.
[34] A. A. Kosterev and F. K. Tittel, *Ammonia detection by use of quartz-enhanced photoa-*

coustic spectroscopy with a near-IR telecommunication diode laser, Appl. Opt., 43 (2004), pp. 6213–6217.

[35] A. A. Kosterev, F. K. Tittel, D. V. Serebryakov, A. L. Malinovsky, and I. V. Morozov, *Applications of quartz tuning forks in spectroscopic gas sensing*, Rev. Sci. Instrum., 76 (2005), 043105.

[36] M. Lassas and E. Somersalo, *On the existence and convergence of the solution of PML equations*, Computing, 60 (1998), pp. 229–241.

[37] F. Magoulès, P. Iványi, and B. Topping, *Non-overlapping Schwarz methods with optimized transmission conditions for the Helmholtz equation*, Comput. Methods Appl. Mech. Engrg., 193 (2004), pp. 4797–4818.

[38] P. Martinsson, *A direct solver for variable coefficient elliptic PDEs discretized via a composite spectral collocation method*, J. Comput. Phys., 242 (2013), pp. 460–479.

[39] T. Mary, *Low-Rank Multifrontal Solvers: Complexity, Performance, and Scalability*, Ph.D. thesis, University of Toulouse, Toulouse, France, 2017.

[40] A. Miklós, P. Hess, and Z. Bozóki, *Application of acoustic resonators in photoacoustic trace gas analysis and metrology*, Rev. Sci. Instrum., 72 (2001), pp. 1937–1955.

[41] A. Miklós, S. Schäfer, and P. Hess, *Photoacoustic spectroscopy, theory*, in Encyclopedia of Spectroscopy and Spectrometry, Vol. 3, J. C. Lindon, G. E. Tranter, and J. L. Holmes, eds., Academic Press, London, 2000, pp. 1815–1822.

[42] P. Morse and K. Ingard, *Theoretical Acoustics*, McGraw–Hill, New York, 1968.

[43] M. F. Murphy, G. H. Golub, and A. J. Wathen, *A note on preconditioning for indefinite linear systems*, SIAM J. Sci. Comput., 21 (2000), pp. 1969–1972, https://doi.org/10.1137/S1064827599355153.

[44] H. Nouira, E. Foltête, L. Hirsinger, and S. Ballandras, *Investigation of the effects of air on the dynamic behavior of a small cantilever beam*, J. Sound Vib., 305 (2007), pp. 243–260.

[45] J. Nye, *Physical Properties of Crystals*, Oxford University Press, New York, 2000.

[46] P. Patimisco, G. Scamarcio, F. K. Tittel, and V. Spagnolo, *Quartz-enhanced photoacoustic spectroscopy: A review*, Sensors, 14 (2014), pp. 6165–6206.

[47] J. C. Petersen, L. Lamard, Y. Feng, J.-F. Focant, A. Peremans, and M. Lassen, *Quartz-Enhanced Photo-acoustic Spectroscopy for Breath Analyses*, Proc. SPIE 10055, 2017.

[48] N. Petra, J. Zweck, A. A. Kosterev, S. E. Minkoff, and D. Thomazy, *Theoretical analysis of a quartz-enhanced photoacoustic spectroscopy sensor*, Appl. Phys. B, 94 (2009), pp. 673–680.

[49] N. Petra, J. Zweck, S. E. Minkoff, A. A. Kosterev, and J. H. Doty III, *Modeling and design optimization of a resonant optothermoacoustic trace gas sensor*, SIAM J. Appl. Math., 71 (2011), pp. 309–332, https://doi.org/10.1137/100807181.

[50] J. Poulson, B. Engquist, S. Li, and L. Ying, *A parallel sweeping preconditioner for heterogeneous* 3*D Helmholtz equations*, SIAM J. Sci. Comput., 35 (2013), pp. C194–C212, https://doi.org/10.1137/120871985.

[51] A. Quarteroni and A. Valli, *Domain Decomposition Methods for Partial Differential Equations*, The Clarendon Press, Oxford University Press, New York, 1999.

[52] Y. Saad, *Iterative Methods for Sparse Linear Systems*, 2nd ed., SIAM, Philadelphia, 2003, https://doi.org/10.1137/1.9780898718003.

[53] A. Siegman, *Lasers*, University Science Books, Oxford, UK, 1986.

[54] S. Wang, X. S. Li, F.-H. Rouet, J. Xia, and M. V. De Hoop, *A parallel geometric multifrontal solver using hierarchically semiseparable structure*, ACM Trans. Math. Software, 42 (2016), 21.

[55] H. Zheng, X. Yin, L. Dong, H. Wu, X. Liu, W. Ma, L. Zhang, W. Yin, and S. Jia, *Multi-quartz enhanced photoacoustic spectroscopy with different acoustic microresonator configurations*, J. Spectros., 2015 (2015), 218413.

[56] X. Zuo, Z. Mo, T. Gu, X. Xu, and A. Zhang, *Multi-core parallel robust structured multifrontal factorization method for large discretized PDEs*, J. Comput. Appl. Math., 296 (2016), pp. 36–46.